

Surface plasmon band tailoring of plasmonic nanostructure under the effect of water radiolysis by synchrotron radiation

Amardeep Bharti,^{a*} Ashish K. Agrawal,^{b,c} Balwant Singh,^{b,c} Sanjeev Gautam^{d*} and Navdeep Goyal^{a*}

Received 20 May 2017

Accepted 14 September 2017

Edited by A. F. Craievich, University of São Paulo, Brazil

Keywords: plasmonic nanostructure; silver nanoparticles; X-rays; Mie theory; water radiolysis.

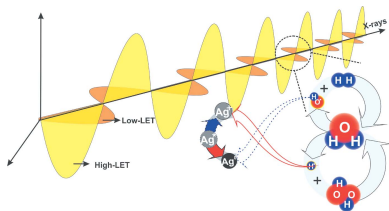
^aDepartment of Physics, Panjab University, Chandigarh 160014, India, ^bTechnical Physics Division, Bhabha Atomic Research Center, Mumbai 400094, India, ^cIndus Synchrotrons Utilization Division, Raja Ramanna Centre for Advanced Technology, Indore 452013, India, and ^dDr S. S. Bhatnagar University Institute of Chemical Engineering and Technology, Panjab University, Chandigarh 160014, India.

*Correspondence e-mail: abharti@pu.ac.in, sgautam@pu.ac.in, ngoyal@pu.ac.in

Plasmonic metal nanostructures have a significant impact on a diverse domain of fields, including photocatalysis, antibacterial, drug vector, biosensors, photovoltaic cell, optical and electronic devices. Metal nanoparticles (MNPs) are the simplest nanostructure promising ultrahigh stability, ease of manufacturing and tunable optical response. Silver nanoparticles (AgNp) dominate in the class of MNPs because of their relatively high abundance, chemical activity and unique physical properties. Although MNPs offer the desired physical properties, most of the synthesis and fabrication methods lag at the electronic grade due to an unbidden secondary product as a result of the direct chemical reduction process. In this paper, a facile protocol is presented for fabricating high-yield *in situ* plasmonic AgNps under monochromatic X-rays irradiation, without the use of any chemical reducing agent which prevents the formation of secondary products. The ascendancy of this protocol is to produce high quantitative yield with control over the reaction rate, particle size and localized surface plasmon resonance response, and also to provide the feasibility for *in situ* characterization. The role of X-ray energy, beam flux and integrated dose towards the fabrication of plasmonic nanostructures has been studied. This experiment extends plasmonic research and provides avenues for upgrading production technologies of MNPs.

1. Introduction

Plasmonic nanostructures are of immense interest in the broad area of science (research and development) and became the fundamental building blocks for the next-generation technology (Ozby, 2006; Atwater & Polman, 2010). Plasmonic nanostructures offer tunable localized surface plasmon resonance energies (Atwater & Polman, 2010), nonlinear optical effects (Barnes *et al.*, 2003; Kauranen & Zayats, 2012) and non-metallic conductivity (Henzler *et al.*, 1998) due to the quantum confinement of the charge carriers in such a small area. Metal nanoparticles are the simplest and most promising plasmonic nanostructures for numerous applications in the fields of microelectronics (Atwater & Polman, 2010), photonics (Ozby, 2006), biotechnology (Bharti *et al.*, 2014, 2016a), *etc.* Bio-body implant and electronic applications require ultrahigh stable and pure material. Infinite efforts had been imparted for the synthesis and fabrication of such plasmonic nanostructures with a wide range of sizes and shapes *via* direct chemical reduction processes (Caldorera-Moore *et al.*, 2010; Sun & Xia, 2002). However, most of these methods lag at



© 2017 International Union of Crystallography

the electronic grade because of low stability and unbidden secondary product contamination.

To control the size and shape of the nano-objects, one has to control the reaction rate and the surrounding chemical environment (Sun & Xia, 2002). In the direct chemical reduction method, the reaction rate has been controlled by the addition of some inhibitor agent (Chu *et al.*, 2006), which may simultaneously produce secondary products.

During the last two decades, radiation physicists and chemists have indulged in the formation of plasmonic nanostructures by means of radiolysis through ionizing radiation (Abedini *et al.*, 2013; Remita *et al.*, 2005; Belloni *et al.*, 1998) (*i.e.* electron, proton, gamma and X-ray beams). Ionizing radiation causes the decomposition of water and produces hydrated electrons (e_{aq}^-), atom radicals (H^\bullet) and superoxides (O_2^-) which are strong reducing agents of metal salts (Abedini *et al.*, 2013). X-rays dominate in this class because of their availability in the laboratory and at synchrotron light sources. X-rays promise longer exposures as well as *in situ* characterization which can lead to an understanding of the nature of nanostructures as they grow simultaneously (Remita *et al.*, 2007). Numerous research activities have been performed using X-rays in the synthesis and characterization of nanomaterials. X-ray irradiation also leads to chemical enhancement of nanomaterials (Cheng *et al.*, 2012). Many research groups successfully demonstrate the synthesis of metal nanoparticles using ‘white’ X-rays, but the ‘monochromatic’ X-rays role is rarely reported. Monochromatic X-rays provide the feasibility to investigate the real-time evolution of particle size, morphology, and electronic and crystalline structure (Sun & Ren, 2013). This unique feature of ‘monochromatic’ X-rays gains remarkable interest in the production of plasmonic nanostructures.

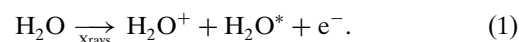
We have recently shown that the monochromatic X-ray beam induced radiolysis of water leads to the reduction of metal salt to zero-valent metal nanoparticles (Bharti *et al.*, 2016b). The synthesized plasmonic nanoparticles have ultra-high stability and are free from any secondary product contaminations (Bharti *et al.*, 2016b). In this paper, we report the detailed analysis of the role of ‘monochromatic’ X-ray energy, beam flux and integrated dose towards the fabrication of plasmonic nanostructures *via* water radiolysis. The optical properties of nanostructures were investigated by UV-visible spectroscopy.

2. Water radiolysis

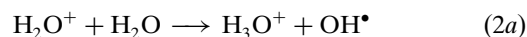
Electrolysis was discovered at the end of the 18th century. The electrolysis of water consists of the decomposition (putrefaction) of H_2O into dioxygen (O_2) and dihydrogen (H_2) at the electrodes, as the electric current passes. At present, water decomposition is carried out by the radiolysis process *via* ionizing radiation, *i.e.* radiation from the decay of radioactive materials, accelerated charged particles (*e.g.* electrons, protons and ions) and X-rays (Caer, 2011; Jonah, 1995; Giesel, 1902; Kernbaum, 1909).

Studies of the chemical effects of high-energy ionizing radiation were accelerated by the discovery of X-rays by Röntgen in 1895. Giesel, Marie Curie and Kernbaum were the first to experimentally prove the putrefaction of water by ionizing radiation (Giesel, 1902; Kernbaum, 1909). Andre Debierne was the first to give a hypothesis for the production of the H^\bullet atom and OH^\bullet radical during the radiolysis of water (Debierne, 1914). Rise and Fricke showed that radiation induces the ‘activated water’ which interacts with the solute, if the concentration of solute is adequate; otherwise it would decay back to a water molecule (Fricke, 1935). Later, Milton Burton’s group confirmed the production of such and the mechanisms were then explained by Allen (1948). Allen suggested that the molecular yields stem from the H^\bullet and OH^\bullet radical recombination eventuate in the vicinity of high radical concentration (HRC). Radicals which elude from the vicinity of HRC would diffuse and chemically react with solute (Allen, 1948). Milton Burton’s proposed the ‘G-value’ (SI unit is Gray) which denotes the number of molecules generated and destroyed per 100 eV of radiation energy imparted to the system (Caer, 2011). The water putrefaction is governed around the path of ionizing particles (the so-called track) and is directly proportional to the linear energy transfer (LET = $-dE/dl$) in the medium per unit path length (Jonah, 1995; Samuel & Magee, 1953).

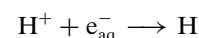
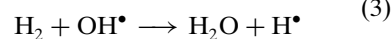
The mechanism of water radiolysis consists of three stages. (i) The physical stage (1 fs): involves energy deposition by ionizing particles through the fast relaxation process and leads to the generation of sub-excitation electrons, excited and ionized water molecules,

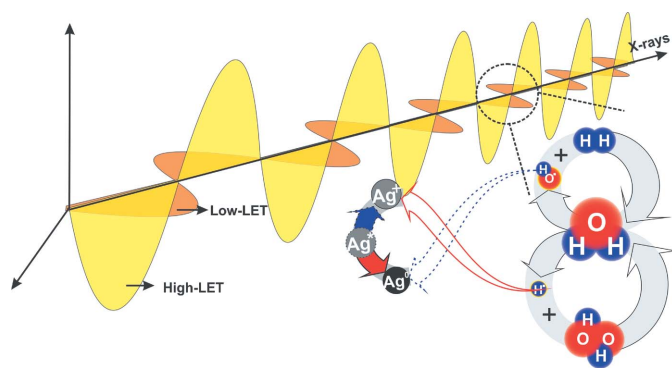


(ii) Physico-chemical stage (10^{-15} – 10^{-12} s): this is the most important stage of water radiolysis. The majority of the radicals are generated in this time interval *via* numerous reactions including (a) ion–molecule reaction, (b) dissociate relaxation, (c) auto-ionization of excited states, (d) solvation of electrons, (e) hole diffusion, *etc.*



(iii) Chemical stage (10^{-12} – 10^{-6} s): involves the recombination and diffusion of the generated product in the solution which reacts with solute, resulting in the formation of tracks,

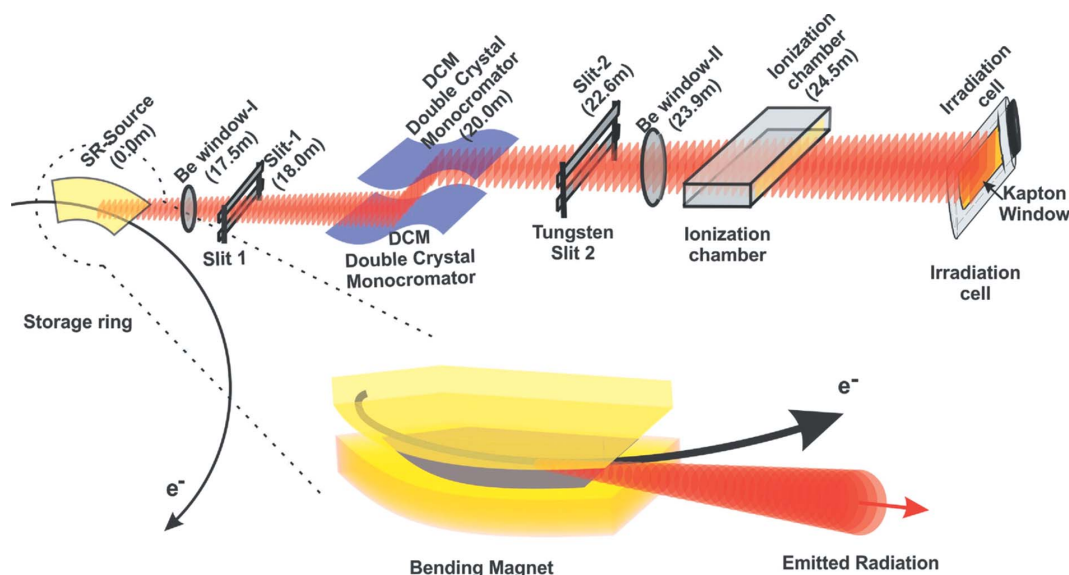
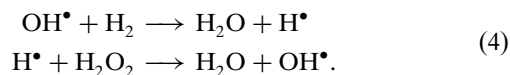



Figure 1

Pictorial representation of the X-ray induced conversion of metallic ions into zero-valent nanoparticles *via* water radiolysis. Sinusoidal waves describe the linear energy transfer strength of X-rays in water. X-rays decompose the water into H^\bullet and OH^\bullet radicals and H_2 and H_2O_2 molecules making an eight-loop reaction. H^\bullet is a strong reducing agent that converts Ag^+ to Ag^0 within its vicinity.

In the case of low-LET irradiation, the probability of recombination is negligible after $1 \mu\text{s}$ (Caer, 2011). The molecular products yield is directly dependent on LET whereas radicals are indirectly dependent, because of the enhanced ionization in the tracks (LaVerne & Schuler, 1983). Thus, high-LET particles lead to the recombination of radicals which produce molecular products. Low-LET irradiation proceeds to eight-loop reactions causing the generation of water molecules again as shown in Fig. 1.

This loop reaction is mediated by the H^\bullet atom and OH^\bullet radicals and the destruction rate of the molecular products is equal to their generation rate,


Figure 2

Optical layout of the Indus-2 BL-04 beamline showing the relative distance of each component from the tangent point. The inset describes the generation of X-rays by a bending electron beam under the effect of a magnetic field. Beam energy has been tuned using a parallel double-crystal monochromator [Si(111)] in the range 8–35 keV.

Aqueous electrons (e_{aq}^-) and atom radicals (H^\bullet) are strong reducing agents towards the metal salt with standard potential $E_0(\text{H}_2\text{O}/e_{\text{aq}}^-) = -2.9 \text{ V}_{\text{NHE}}$ and $E_0(\text{H}^+/\text{H}^\bullet) = -2.3 \text{ V}_{\text{NHE}}$, respectively; whereas hydroxyl radicals (OH^\bullet) are strong oxidant agents with standard potential $E_0(\text{HO}^\bullet/\text{H}_2\text{O}) = +2.7 \text{ V}_{\text{NHE}}$ (Caer, 2011). We have performed the experiment in the specially designed closed irradiation cell, so that the dihydrogen H_2 could not escape and prevent the accumulation of oxidant (O_2 , H_2O_2) products.

3. Indus-2 synchrotron and beamline description

Indus-2 is a third-generation synchrotron light source. The electron beam is generated by a 20 MeV microtron operated at 30 mA. Lanthanum hexaboride (LaB_6) serves as a source for the electron emitter. The synchrotron is basically a cyclotron accelerator in which the magnetic field strength is calibrated with the energy of accelerated charged particles to keep their orbital radius constant. A detailed history of synchrotron radiation is given by Blewett (1998).

The full-field hard X-ray imaging beamline (BL-04) at the 10° port of the bending-magnet DP-2 of Indus-2 is operated in monochromatic and white-beam modes (Agrawal *et al.*, 2015). The optical layout of the beamline and the relative distances of its components from the tangent point are illustrated in Fig. 2.

The beamline is composed of four hutches, *i.e.* the front-end, optics, experimental station and control room hutches. The front-end structure consists of a collimator, beam monitor, mask and safety shutter. The optics hutche is operated under ultra-high vacuum (10^{-9} mbar). It is designed to prepare the beam by collimation, filtering and energy tuning as per experimental requirements. A parallel double-crystal monochromator [DCM-Si(111)] has been used to tune the

energy in the range 8–35 keV (Agrawal *et al.*, 2015). Instrumentation required for beam diagnostics and the safety system is installed in the optics hutch. Major components of the beamline are water-cooled and their temperatures are measured continuously *via* thermocouples installed in the respective devices (Raghuvanshi *et al.*, 2007). The data are used as feedback for the equipment protection system (EPS) of the beamline to operate its components under safe conditions and to avoid any possibility of excessive heating or contamination (Agrawal *et al.*, 2015; Raghuvanshi *et al.*, 2007). The experimental station consists of all the instruments required for sample holding, manipulation and alignment, imaging detectors, data acquisition electronics, beam analysis, vibration-free optical tables *etc.* (Agrawal *et al.*, 2015).

4. Theoretical approach to the optical properties of metal nanoparticles: ‘Mie theory’

Size- and shape-dependent optical properties of the metal nanostructures related to plasmon excitation are the keen interest of microelectronic and photonic research from the last three decades. More precisely, the UV–visible absorption spectra of metal nanoparticles in the solution phase can be simulated by ‘Mie theory’ using their wavelength-dependent optical constants relating to the surrounding media (Petit *et al.*, 1993). For smaller particles (<20 nm) the dipole term of the Mie summation directly contributes to the absorption spectra. If the particles are considered to be spherical of volume V with a dispersion of N particles per unit volume, the absorbance is described by (Petit *et al.*, 1993)

$$A = \sigma_{\text{abs}} Nl/2.303, \quad (5)$$

where l is the optical path length and σ_{abs} is the absorption cross section given by

$$\sigma_{\text{abs}} = 18\pi V \varepsilon(\omega)^2 / \lambda \{ [\varepsilon_1(\omega) + 2\varepsilon_m]^2 + \varepsilon_2(\omega)^2 \}, \quad (6)$$

where λ is the incident light wavelength and $\varepsilon(\omega) = \varepsilon_1(\omega) + i\varepsilon_2(\omega)$ is the complex permittivity of the metal relative to the surrounding medium which implies that the maxima in the absorption would occur at the Fröhlich frequency $\varepsilon_1(\omega) = -2\varepsilon_m$ (dielectric function of the surrounding media). The corresponding wavelength of this plasma resonance is governed by the real part of the dielectric function $[\varepsilon_1(\omega)]$ of the metal (Pathak & Sharma, 2016). The broadening and the intensity of the plasmon resonance peak is determined by the imaginary part $\varepsilon_2(\omega)$ at the resonance. In the case of silver, the real dielectric part is the linear function of the frequency which results in the Lorentzian-shaped absorption band.

In the case of metals, for the free-electron sea the dielectric function is governed by the Drude model as (Pathak & Sharma, 2016)

$$\varepsilon(\omega) = 1 - \frac{\omega_p^2}{\omega^2 + i\omega\gamma}, \quad (7)$$

where ω_p is the plasma frequency ($1.38 \times 10^{16} \text{ s}^{-1}$) and γ is the Drude phenomenological damping constant which is equal to the bandwidth of the dipole plasmon polariton. In the case of

free electrons the classical theory of metals deduces that γ is due to photon scattering with electrons and is related to the mean free path of electrons, which is strongly affected by particle size (Pathak & Sharma, 2016). For particles smaller than the mean free path of conduction electrons in the bulk, γ is increased due to additional collisions with the particles’ boundaries and formulated by the expanded version of Mie theory as (Pathak & Sharma, 2016)

$$\gamma(r) = \gamma_0 - \frac{v_f}{L} = \gamma_0 - C \frac{v_f}{r}, \quad (8)$$

where v_f is the Fermi velocity ($1.4 \times 10^6 \text{ m s}^{-1}$) and L is the effective mean free path of the collisions with the boundaries in the bulk material. C is a constant that attributes to the diffuse scattering process (0.75 for Ag) and γ_0 is the damping of bulk scattering ($5 \times 10^{12} \text{ s}^{-1}$). Using the above formulations the ‘size’ of the nanoparticles from extinction spectra has been deduced.

5. Methods

All the chemicals of high-purity grade were purchased from Sigma Aldrich. AgNO_3 and polyvinylpyrrolidone (PVP) serve as precursor and capping agent, respectively. Precursor solution was irradiated by synchrotron X-rays in a specially designed polypropylene cell having kapton windows.

The integrated dose has been calculated using the expression

$$ID_{\text{integrated dose}} = \frac{E \Phi_{\text{ph}} \% \text{absorption}}{d_{\text{cell}} \rho_{\text{sample}}} T_{\text{irradiation time}}, \quad (9)$$

as discussed by Bharti *et al.* (2016b), where E is the photon energy, Φ_{ph} is the photon flux density, d_{cell} is the cell thickness, ρ_{sample} is the sample density and T is the irradiation time. Graphs showing the absorption of X-rays by water molecules and cross-section area variation with respect to photon energy are given in Fig. 3. Due to the current decay mode of Indus-2, several correction factors are required for the calculation of the integrated irradiation dose, as the flux density has a direct dependence on the beam current as (Hulbert & Weber, 1992; Schwinger, 1949)

$$\frac{d^2 \Phi_{\text{ph}}(\omega)}{d\theta d\Psi} = \frac{3\alpha}{4\pi^2} \ell^2 \frac{\Delta\omega}{\omega} \frac{I}{e} y^2 (1 + X^2)^2 \times \left[K_{2/3}^2(\xi) + \frac{X^2}{1 + X^2} K_{1/3}^2(\xi) \right], \quad (10)$$

where θ and Ψ are the observatory angle in the horizontal and vertical planes, respectively, α is the fine structure constant, ℓ is the electron energy, ω is the photon angular frequency, I is the beam current, e is the electron charge, $y = \omega/\omega_c$ ($\omega_c = 3\ell^2 c/2\rho$), ρ is the radius of curvature of the e^- trajectory ($= E/ecB$ where E is the electron beam energy), $X = \ell\Psi$ and $\xi = y(1 + X^2)^{3/2}/2$. The resultant of this equation in the horizontal plane ($\Psi = 0$) and in practical units of flux [photons $\text{s}^{-1} \text{ mrad}^{-1}$ ($0.1\% \text{ bandwidth}^{-1}$)] comes out to be (Hulbert & Weber, 1992)

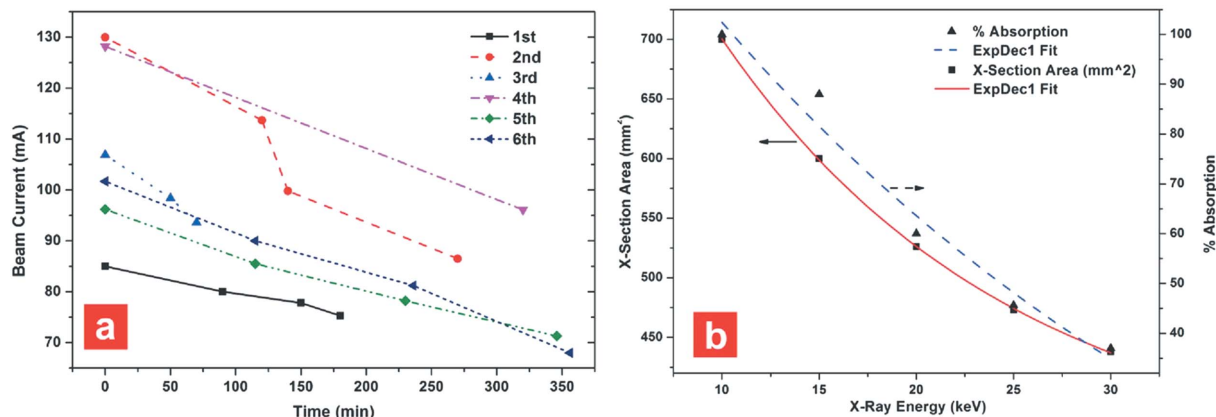


Figure 3 (a) Beam current decay rate as a function of time due to electron loss in the synchrotron. (b) Beam cross-section variation and the percentage absorption of X-rays by water molecules at various energies.

$$\frac{d\Phi_{ph}(y)}{d\theta} = 2.457 \times 10^{13} E [\text{GeV}] I [\text{A}] G_1(Y), \quad (11)$$

where

$$G_1(Y) = y \int_y^\infty K_{5/3}(y') dy'$$

The slope of the current decay rate during the experiments was almost constant as shown in Fig. 3(a). Because of the current decay in the accelerated beam over time, the flux has been theoretically calculated as a function of photon energy at a sample holder stage 25 m from the tangent point of the bending magnet, by proper selection of incident beam divergence using the *XOP* code (Sanchez del Rio & Dejus, 2004). Fig. 4(a) shows a comparison of the theoretical and experi-

mental flux in the photon energy range used in the experiments. The one order difference in the photon flux is due to the attenuation and scattering losses by beamline optical components, *i.e.* DCM, Be windows, ion chamber, air, *etc.* (Agrawal *et al.*, 2015). So the correction factor for the transmission of the X-ray beam through 2×0.4 mm Be windows, 10 cm Ar ion chamber, 110 cm air path and 0.03 mm Kapton window has been incorporated as shown in Fig. 4(b). Therefore the calculated flux $\times 0.92$ [Be] $\times 0.26$ [Ar] $\times 0.53$ [Air] $\times 0.98$ [Kapton] = 2.35×10^8 photons $\text{s}^{-1} \text{mm}^{-2}$ at 10 keV is quite comparable with the measured 1.8×10^8 photons $\text{s}^{-1} \text{mm}^{-2}$ flux. The small difference is due to the energy-dependent absorption and scattering losses during monochromatization of the beam at the DCM. So the flux density has been calculated as a function of beam current as shown in Fig. 4(c) and used after applying the above correction for integrated dose calculations.

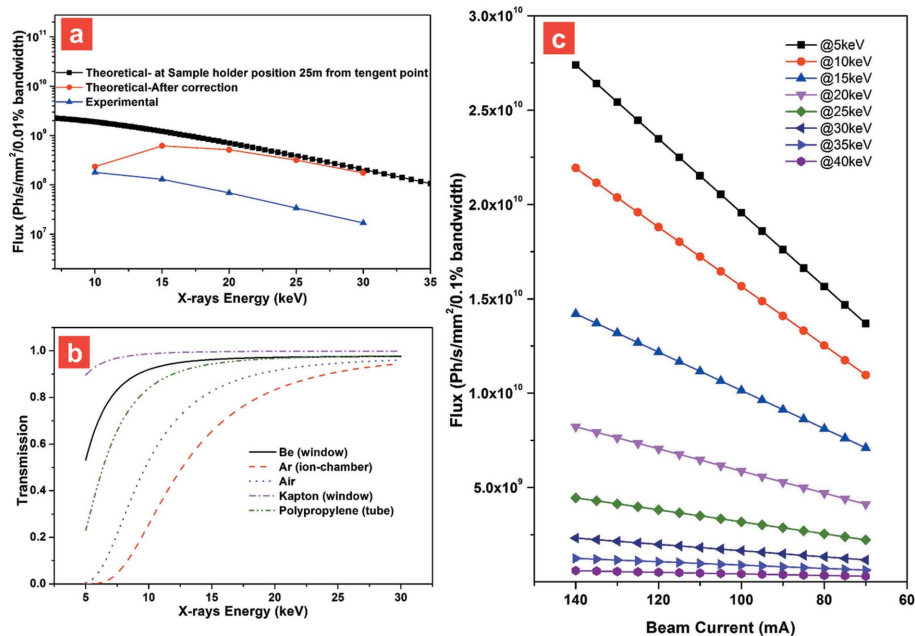


Figure 4 (a) Comparison of monochromatic beam flux variation calculated using a theoretical approach with measured data at various photon energies. (b) X-ray transmission through different beamline components as a function of photon energy. (c) Theoretically calculated flux density of the monochromatic beam as a function of beam current decay.

6. Results and discussions

6.1. Effect of X-ray energy on the fabrication of plasmonic nanostructures

To study the effect of X-ray energy on the fabrication of plasmonic nanostructures, a precursor sample (AgNO_3 : PVP 1:1 by weight) was irradiated under varying X-ray energy at constant integrated dose. The colour change from transparent to yellow is the first confirmation of the production of plasmonic nanostructures as shown in the inset of Fig. 5(a). From the extinction spectra of the prepared samples (Fig. 5a) we have observed the two phenomena affected by X-ray energy. First, an increase in X-ray energy leads to an enhanced LET resulting in a higher yield of hydrated e_{aq}^- . Reduction of the

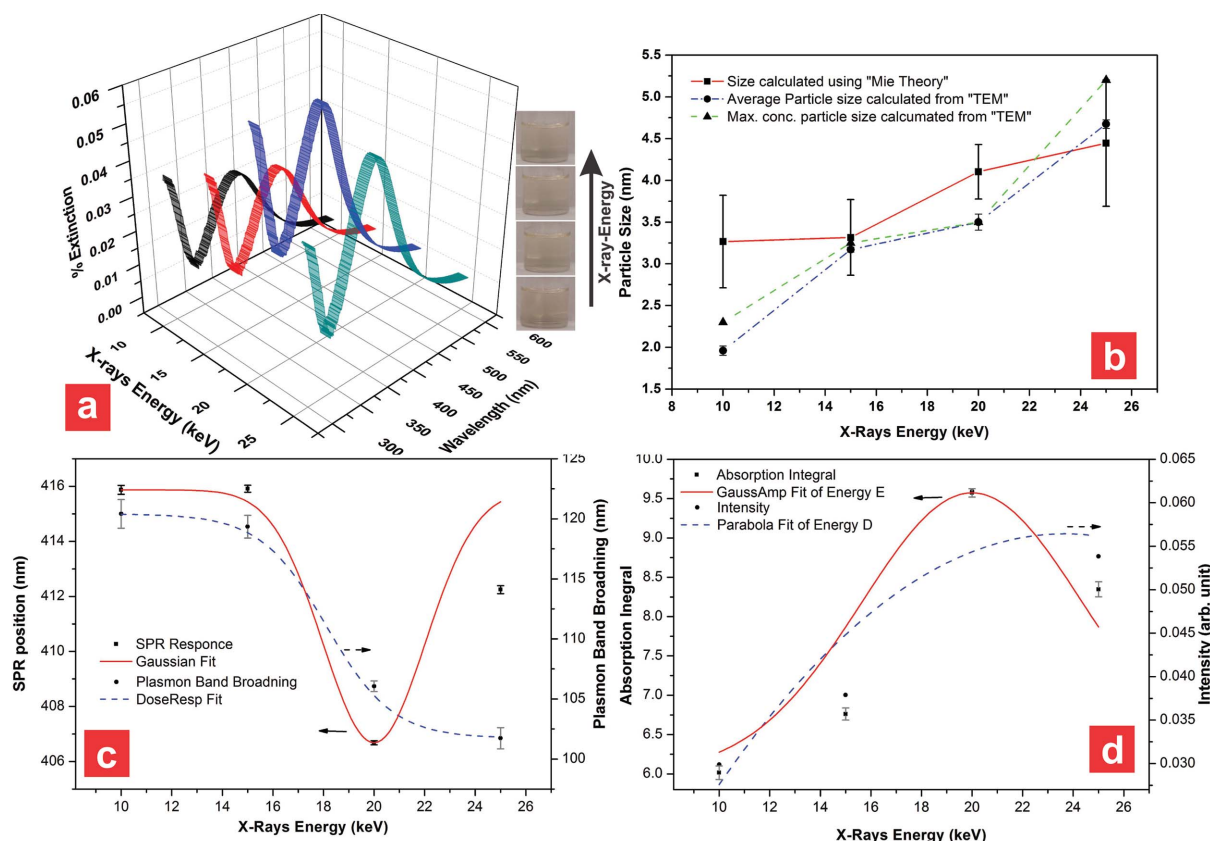
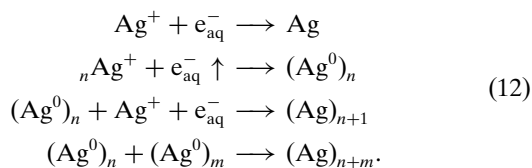


Figure 5 (a) Extinction spectra of the samples synthesized using water radiolysis by varying X-ray energy at constant integrated dose (the inset shows the yellow colour appearance). (b) Theoretically calculated particle size using Mie theory as a function of X-ray energy. (c, d). Fitting of detailed parameters (SPR position, PBB, absorption integral and band intensity) of extinction spectra with varying X-ray energy.

metal salt boost in the vicinity of the longer impact of atom radicals (Jonah, 1995) results in the growth of particle size as depicted by the theoretical fit of the Mie theory shown in Fig. 5(b),



Second, as the energy increases, the target becomes more transparent to the beam and more time is required to achieve the desired integrated-dose value. Absorption integral spectra reveal a loss in X-ray absorption degraded particle yield after a certain energy value as shown in Figs. 5(c) and 5(d).

Information regarding the particle size and its distribution can be deduced from the surface plasmon resonance (SPR) position and plasmon-band broadening (PBB) (Petit *et al.*, 1993). The SPR position is co-related to the size-dependent effective dielectric behaviour of the metal nanoparticles due to the interaction of the conducting electrons because of quantum confinement at the nano-scale (Pathak & Sharma, 2016). In the case of nanoparticles, their dimensions are equivalent to the effective mean free path of electrons in bulk, which leads to scattering of the electrons from the particle

surface, resulting in the localized surface plasmon resonance response. A change in the surface-to-volume ratio affects the dielectric constant of nanoparticles due to the electromagnetic interaction between neighbouring grain boundaries which leads to a shift in the SPR position. This shift is due to the separation between the induced charges at opposite interfaces which increases with particle size, and thus led to a lower restoring force implying resonance at lower frequency. On the other hand, an increase in the surface-to-volume ratio leads to the oscillating electrons possessing a higher probability of being scattered at the particle surface. This enhanced scattering reduces the lifetime of the oscillation and hence increases the PBB.

According to Mie theory, multiplication in the plasmon resonance response is due to anisotropic effects present in the nanostructure (Singh *et al.*, 2015). In this case, the extinction spectrum shows a single plasmon band that confirms the ‘isotropic’ nature of the plasmonic nanostructure. The maxima in SPR between 400 and 420 nm are attributed to the transverse oscillation of electrons due to absorption as well as scattering of light, and the minimum at ~337 nm is due to the imaginary part of the refractive index $\{n_{\text{Im}} = \text{Im}[\epsilon(\lambda)]^{1/2} \simeq 0.4$ for bulk Ag} (Singh *et al.*, 2015). The PBB at the longer wavelength is related to the particle size distribution in the sample. According to Mie theory, SPR and PBB should follow a very similar route, but Fig. 5(c) depicts disorder at higher

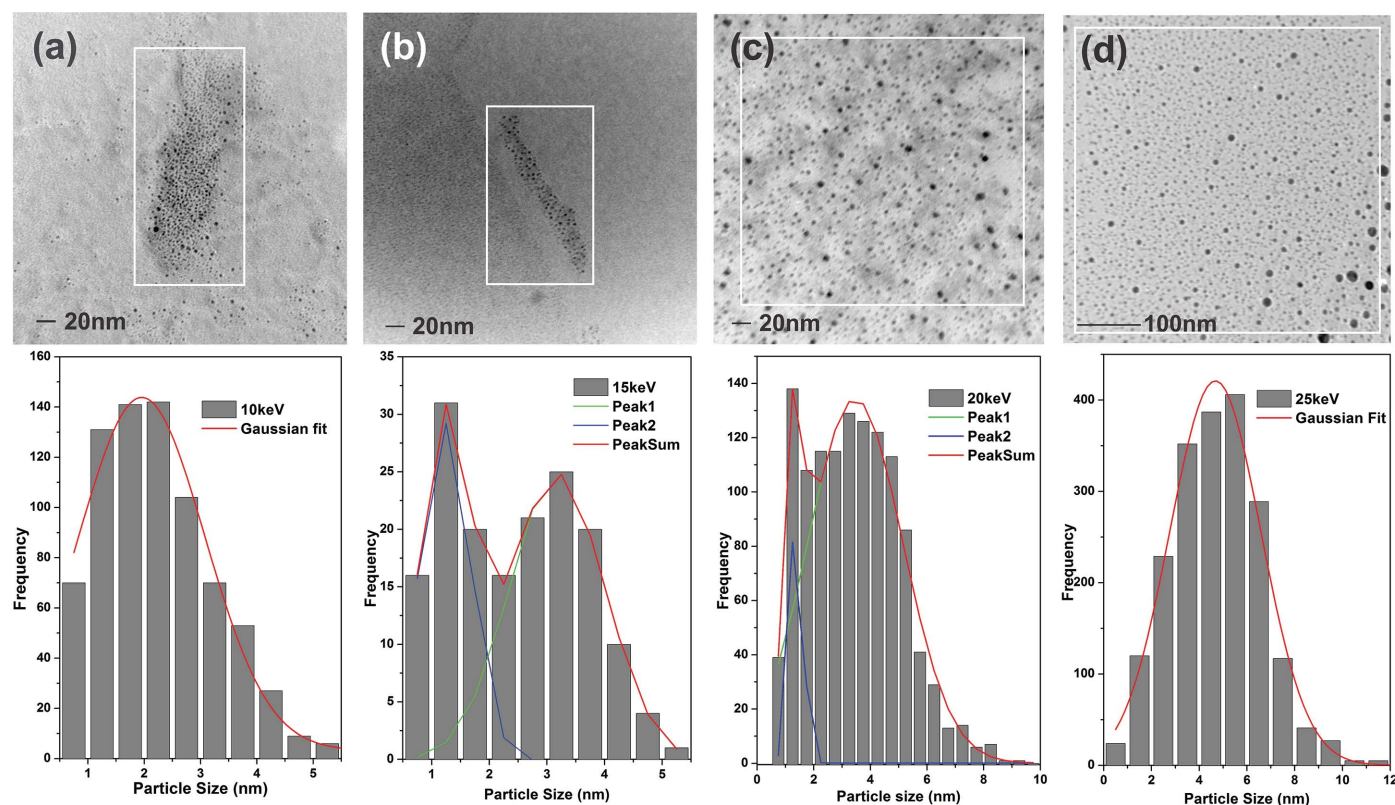


Figure 6

Top: electron micrographs of samples prepared under the irradiation of varying X-ray energy [(a) 10 keV, (b) 15 keV, (c) 20 keV, (d) 25 keV] along with the respective particle size histogram (bottom).

energy because of the absorption loss. Transmission electron micrographs (TEMs) of samples prepared under the irradiation of varying X-ray energy confirm the formation of spherical nanoparticles without any coagulation as shown in Fig. 6. A size distribution histogram has been deduced from the corresponding electron micrographs using an image processing tool (*ImageJ* 1.41o). The TEM histogram supports the 'particle size' profile as a function of X-ray 'energy' as depicted by Mie theory shown in Fig. 5(b).

So the 'energy' selection for this type of experiment depends upon the beam flux, beam cross section and the sample holder size. As in the case of this experiment, Figs. 5(c) and 5(d) show that a 20 keV X-ray beam is dominated by the production of higher yield plasmonic nanostructures.

6.2. Effect of integrated dose on the fabrication of plasmonic nanostructure

The effect of the integrated dose has been studied by exposing the samples under varying irradiation times at 20 keV. The integrated dose is directly proportional to the beam energy absorption in the sample. The integrated dose has been calculated using the above-mentioned formulae. The simulated photon flux is well matched with the experimentally measured flux profile with varying X-ray energy as shown in Fig. 4(a). Therefore, a beam-current-dependent profile for the photon flux has been obtained by varying the current at constant X-ray energy using *XOP*. The theoretically calcu-

lated beam flux as a function of beam current has been incorporated into the calculations as discussed in §5. The higher the integrated dose imparted to the system, the higher will be the production of atom radicals which would enhance the metal salt (M^+) reduction to the zero-valent (M^0) particles (LaVerne & Schuler, 1983). Fig. 7(a1) shows extinction spectra of the samples formed under the exposure of 20 keV monochromatic X-rays at varying irradiation times. The increase in integrated dose enhances atom radical production which triggers the metal salt reduction process and leads to the exponential growth of particle size as shown in Fig. 7(b1). The close fit of the SPR and PBB as a function of integrated dose strongly approves the Mie fitting as shown in Fig. 7(c1).

6.3. Effect of chemical content on the fabrication of plasmonic nanostructure

In the case of zero-valent metal nanoparticles, capping agents play a vital role in preventing the oxidation of M^0 back to M^+ . The radiolysis of water not only produces (e_{aq}^- , H^\bullet , O_2^-) reducing agents but simultaneously the (OH^\bullet) oxidizing agent (Debiere, 1914). Superoxide O_2^- has a complex nature regarding its reaction with metal salt: its role as a reducing or oxidizing agent depends upon the oxidation state of the metal. O_2^- donates an electron to metals of higher oxidation state and receive an electron from those of lower oxidation state (Wishart & Rao, 2010). Therefore, in the case of noble metals, O_2^- serves as a reducing agent. OH^\bullet causes the reverse order

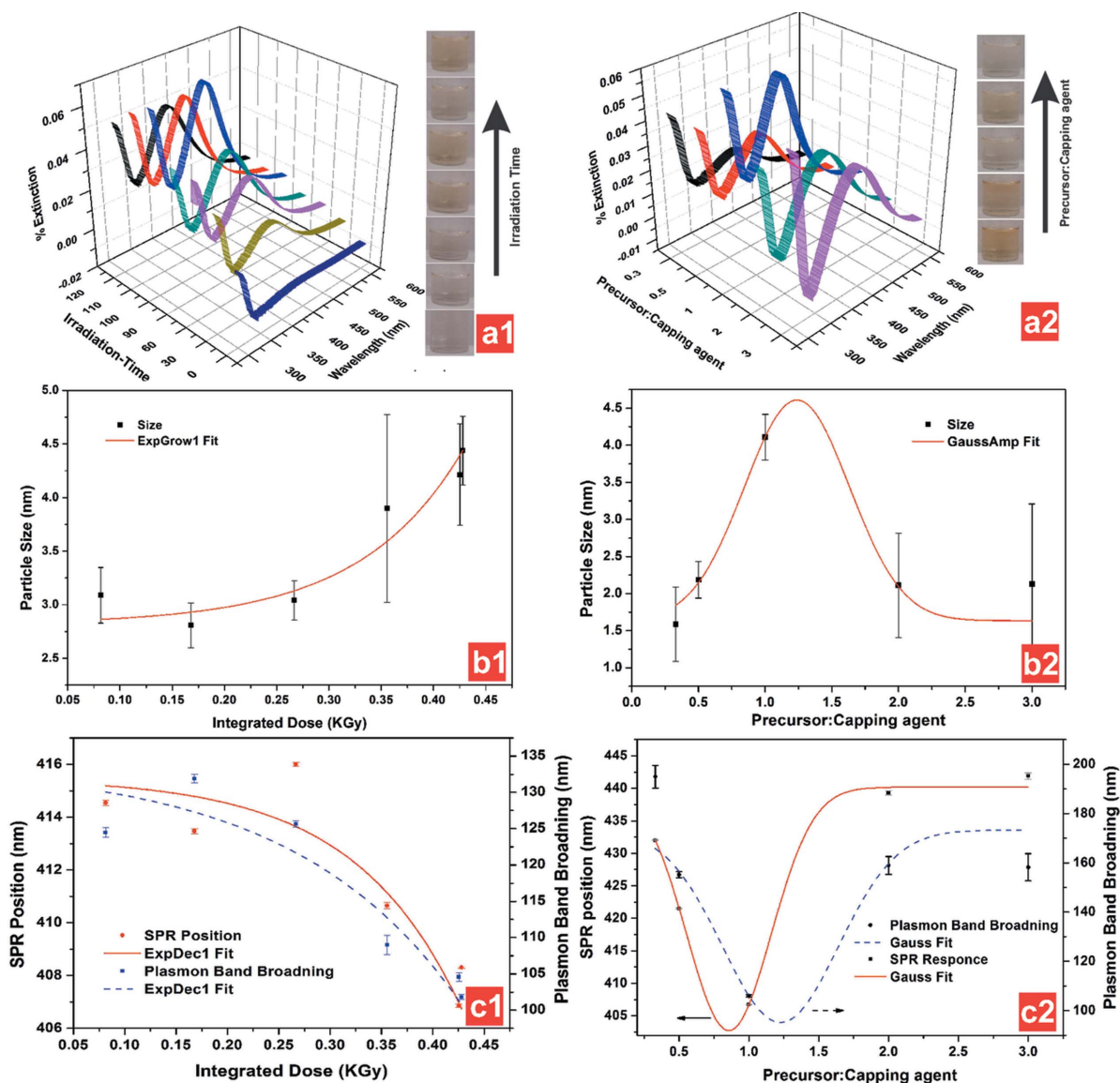
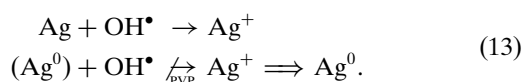


Figure 7 Extinction spectra of the samples synthesized under irradiation of a monochromatic X-ray beam by (a1) varying the irradiation time at 20 keV and (a2) varying the relative concentration of the precursor and capping agent at 20 keV. (b1, b2) Fitting of the particle size growth calculated using Mie theory. (c1, c2) Fitting of the SPR position and PBB.

reaction *via* oxidation of Ag^0 to Ag^+ . But the probability of this event decays as the concentration of (e_{aq}^- , H^\bullet , O_2^-) dominates over OH^\bullet radicals (Bharti *et al.*, 2016b). Moreover, PVP has enough ability to cap the synthesized nanostructure and prevent oxidation (Bharti *et al.*, 2016b; Koczur *et al.*, 2015),



So it is necessary to investigate the effect of the relative ratio of the precursor to capping agent. Samples of different precursor/capping agent ratio (PCR) have been irradiated under constant integrated dose of 20 keV X-ray beam. In Fig. 7(a2) the characteristic AgNp band between 400 and 450 nm in the extinction spectra confirms the formation of plasmonic nanostructures at all PCR. Figs. 7(b2) and 7(c2) reveal that the particle size and the yield are at the utmost

level of the moderate PCR value. It is interesting to note that the particle size becomes smaller at lower and higher PCR, though the phenomena/theories behind these effects are different: at lower PCR the particle size is smaller due to the relatively strong binding of the capping agent, whereas at higher PCR it is smaller due to the relatively enhanced oxidation process at low capping agent concentration.

7. Conclusion

The presented results show a novel protocol for the fabrication of high-yield plasmonic nanostructure under the effect of water radiolysis by synchrotron monochromatic X-rays. The X-rays decomposed the water molecules to atom radicals which act as a reducing agent towards the metal salt. This work delivers a simple synthesis protocol for the production of

ultrapure AgNP without using any chemical reducing agent, which prevents the production of secondary products as in the case of direct chemical reduction. So the synthesized AgNPs are suitable for use in biological and electronic devices. Results show that the size of the plasmonic nanostructure could be tailored by optimizing the X-ray energy, flux and the integrated dose. This experiment investigates a wide range of X-ray energies, which could lead to the *in situ* characterization (SAXS, WAXS, EXAFS, etc.) of materials through which one could easily tailor nanoparticles of their interest.

Acknowledgements

The authors are thankful to Raja Ramanna Centre for Advanced Technology for providing the synchrotron beam time support along with Indus-II staff during the experiment. The authors are also thankful to Dr Ravindra D. Makde (RRCAT) for providing the optical characterization tool. SG acknowledges partial support from UGC-DAE CSR (2014–15/1204) Research Project.

References

- Abedini, A., Daud, A. R., Azmi, M., Hamid, A., Othman, N. K. & Saion, E. (2013). *Nanoscale Res. Lett.* **8**, 474.
- Agrawal, A. K., Singh, B., Kashyap, Y. S., Shukla, M., Sarkar, P. S. & Sinha, A. (2015). *J. Synchrotron Rad.* **22**, 1531–1539.
- Allen, A. O. (1948). *J. Phys. Colloid Chem.* **52**, 479–490.
- Atwater, H. A. & Polman, A. (2010). *Nat. Mater.* **9**, 205–213.
- Barnes, W. L., Dereux, A. & Ebbesen, T. W. (2003). *Nature (London)*, **424**, 824–830.
- Belloni, J., Mostafavi, M., Remita, H., Marignier, J. & Delcourt, M. (1998). *New J. Chem.* **22**, 1239–1255.
- Bharti, A., Bhardwaj, R., Agrawal, A. K., Goyal, N. & Gautam, S. (2016b). *Sci. Rep.* **6**, 22394.
- Bharti, A., Singh, S., Meena, V. K. & Goyal, N. (2014). *Adv. Sci. Lett.* **20**, 1297–1302.
- Bharti, A., Singh, S., Meena, V. K. & Goyal, N. (2016a). *Mater. Today Proc.* **3**, 2113–2120.
- Blewett, J. P. (1998). *J. Synchrotron Rad.* **5**, 135–139.
- Caer, S. L. (2011). *Water.* **3**, 235–253.
- Caldorera-Moore, M., Guimard, N., Shi, L. & Roy, K. (2010). *Expert Opin. Drug Deliv.* **7**, 479–495.
- Cheng, N. N., Starkewolf, Z., Davidson, R. A., Sharmah, A., Lee, C., Lien, J. & Guo, T. (2012). *J. Am. Chem. Soc.* **134**, 1950–1953.
- Chu, H. C., Kuo, C. H. & Huang, M. H. (2006). *Inorg. Chem.* **45**, 808–813.
- Debiere, A. (1914). *Ann. Phys.* **9**, 97–127.
- Fricke, H. (1935). *Cold Spring Harb. Symp. Quant. Biol.* **3**, 55–65.
- Giesel, F. (1902). *Ber. Dtsch. Chem. Ges.* **35**, 3608–3611.
- Henzler, M., Lüer, T. & Burdach, A. (1998). *Phys. Rev. B*, **58**, 10046–10053.
- Hulbert, S. L. & Weber, J. M. (1992). *Nucl. Instrum. Methods Phys. Res. A*, **319**, 25–31.
- Jonah, C. D. (1995). *Radiat. Res.* **144**, 141–147.
- Kauranen, M. & Zayats, A. V. (2012). *Nat. Photon.* **6**, 737–748.
- Kernbaum, M. (1909). *Radium (Paris)*, **6**, 225–228.
- Koczur, K. M., Mourdikoudis, S., Polavarapu, L. & Skrabalak, S. E. (2015). *Dalton Trans.* **44**, 17883–17905.
- LaVerne, J. A. & Schuler, R. H. (1983). *J. Phys. Chem.* **87**, 4564–4565.
- Ozbay, E. (2006). *Science*, **311**, 189–193.
- Pathak, N. K. & Sharma, R. P. (2016). *Plasmonics*, **11**, 713–719.
- Petit, C., Lixon, P. & Pileni, M. P. (1993). *J. Phys. Chem.* **97**, 12974–12983.
- Raghuvanshi, V. K., Dhamgaye, V. P., Singh, A. K. & Nandedkar, R. V. (2007). *AIP Conf. Proc.* **879**, 631–634.
- Remita, S., Fontaine, P., Lacaze, E., Borensztein, Y., Sellame, H., Farha, R., Rochas, C. & Goldmann, M. (2007). *Nucl. Instrum. Methods Phys. Res. B*, **263**, 436–440.
- Remita, H., Lampre, I., Mostafavi, M., Balanzat, E. & Bouffard, S. (2005). *Radiat. Phys. Chem.* **72**, 575–586.
- Sanchez del Rio, M. & Dejus, R. J. (2004). *AIP Conf. Proc.* **705**, 784.
- Samuel, A. H. & Magee, J. L. (1953). *J. Chem. Phys.* **21**, 1080–1087.
- Schwinger, J. (1949). *Phys. Rev.* **75**, 1912–1925.
- Singh, S., Bharti, A. & Meena, V. K. (2015). *J. Mater. Sci. Mater. Electron.* **26**, 3638–3648.
- Sun, Y. & Ren, Y. (2013). *Part. Part. Syst. Charact.* **30**, 399–419.
- Sun, Y. & Xia, Y. (2002). *Science*, **298**, 2176–2179.
- Wishart, J. F. & Rao, B. S. M. (2010). *Recent Trends in Radiation Chemistry*. Singapore: World Scientific.